https://doi.org/10.1016/j.bios.2023.115969

Magnetic-responsive upconversion luminescence resonance energy transfer (LRET) biosensor for ultrasensitive detection of SARS-CoV-2 spike protein

Jiareng Chen,[a] Willis Kwun Hei Ho, [a] Bohan Yin,[a] Qin Zhang,[a] Chuanqi Li,[a] Jiaxiang Yan [a], Yingying Huang[a], Jianhua Hao,[b] Changqing Yi,[c], Yu Zhang,[d] Siu Hong Dexter Wong,[a,*] Mo Yang[a,*]

[a]Department of Biomedical Engineering, the Hong Kong Polytechnic University, Hong Kong 999077, China

[b]Department of Applied Physics, the Hong Kong Polytechnic University, Hong Kong 999077, China

[c]Key Laboratory of Sensing Technology and Biomedical Instruments Guangdong, School of Biomedical Engineering, Sun Yat-Sen University, Guangzhou 510006, China

[d]Department of Mechanical and Automotive Engineering, Royal Melbourne Institute of Technology, Melbourne VIC 3000, Australia

***Corresponding Authors:**

Siu Hong Dexter Wong: shongwong@polyu.edu.hk

Mo Yang: mo.yang@polyu.edu.hk

Abstract

Upconversion nanoparticles (UCNPs) are ideal donors for luminescence resonance energy transfer (LRET)-based biosensors due to their excellent upconversion luminescence properties. However, the relatively large size of antibodies and proteins limits the application of UCNPs-based LRET biosensors in protein detection because the large steric hindrance of proteins leads to low energy transfer efficiency between UCNPs and receptors. Herein, we developed a magnetic responsive UCNPs-based LRET biosensor to control the coupling distance between antibody-functionalized UCNPs (Ab-UCNPs) as donors and antibody-PEG linker-magnetic gold nanoparticles (Ab-PEG-MGNs) as acceptors for ultrasensitive and highly selective detection of SARS-CoV-2 spike proteins. Our results showed that this platform reversibly shortened the coupling distance between UCNPs and MGNs and enhanced the LRET signal with a 10-fold increase in the limit of detection (LOD) from 20.6 pg/mL without magnetic modulation to 2.1 pg/mL with magnetic modulation within 1 hour. The finite-difference time-domain (FDTD) simulation with cyclic distance change confirmed the distance-dependent LRET efficiency under magnetic modulation, which supported the experimental results. Moreover, the applications of this magnetic-responsive UCNP-based LRET biosensor could be extended to other large-size biomolecule detection.

1. Introduction

The 2019 novel coronavirus disease (COVID-19) is a global pandemic caused by severe acute respiratory syndrome coronavirus-2 (SARS-CoV-2). Although the threat

of COVID-19 to humans is fading, new variants are still emerging one after another (Callaway, 2023). It is expected that COVID-19 will become an endemic disease, so low-cost, rapid and sensitive detection of SARS-CoV-2 is still needed.

Nucleic acid detection is the current gold-standard diagnostic method for SARS-CoV-2 detection, mainly based on reverse transcription polymerase chain reaction (RT-PCR) (Kevadiya et al., 2021; Liu et al., 2020a). However, nucleic acid detection suffers the disadvantages of long detection time, the requirement of professionals and complicated equipment, which limits its application, especially in the post- COVID-19 era. The antigen detection method, such as lateral flow assay (LFA), detects the SARS-CoV-2 virus by directly detecting various characteristic proteins, such as spike proteins (SP) on the surface of the virus (He et al., 2023; Mahmoudinobar et al., 2021), which has the advantages of rapid response and high precision. However, the current antigen detection approaches mainly suffer from low sensitivity. A simple, rapid, and sensitive antigen biosensor for SARS-CoV-2 is of high interests for the post- COVID-19 era.

Luminescence resonance energy transfer (LRET)-based biosensors have been developed for various applications, including disease diagnostics (Choi et al., 2021), drug delivery monitoring (Li et al., 2021; Liu et al., 2019; Wang et al., 2021), and mechanobiology studies (Liu et al., 2020b). The efficiency of the process (E) can be calculated by the distance between the donor and the acceptor, typically less than 100 Å (Selvin, 2000). The traditional LRET biosensor is mainly based on organic dyes and fluorescent proteins, which suffer from auto-fluorescence and short fluorescence lifetime (Sapsford et al., 2006). Recently, upconversion nanoparticles (UCNP) have

raised high interests in LRET biosensor due to its NIR excitation, low auto-fluorescence and high signal-to-noise ratio (Wang et al., 2016), which can be good candidates for antigen detection. Another obstacle of the LRET-based biosensors for antigen detection is the distance-dependent energy transfer efficiency between the donors and the acceptors. Most of the current LRET-based biosensors were mainly developed for nucleic acid detection (Song et al., 2022; Tsang et al., 2016), small biomolecule deetction (June et al., 2020) and enzyme activity detection (Kim et al., 2012; Mu et al., 2014). While directly detecting large biomolecules, such as proteins, a relatively long coupling distance between donors and acceptors limit the detection sensitivity due to the large steric hindrance of the proteins and the antibodies.

Hence, we propose a magnetic-responsive upconversion LRET-based biosensor for rapid, sensitive, and selective detection of SARS-CoV-2 S protein with enhanced energy transfer efficiency and sensitivity (Scheme 1). This LRET sensor is established based on a donor-acceptor pair, with UCNPs as donors and magnetic gold nanoparticles (MGNs) as acceptors, where energy is transferred from UCNPs to MGNs via non-radiative dipole-dipole interactions with the conditions that the emission spectrum of the donor overlaps with the absorption spectrum of the acceptor and donor and acceptor are in close distance. Here, MGNs exhibit a broad absorption spectrum overlapping the emission spectrum of the UCNP. To establish the LRET sensing platform, antibody-functionalized UCNP-PEI nanoparticles are firstly conjugated on a glass slide functionalized with the COOH group via EDC/NHS chemistry. In the presence of target S proteins (SPs), antibody-functionalized UCNPs capture SPs and then conjugate with

antibody-PEG linker-magnetic gold nanoparticles (Ab-PEG-MGNs) to form a sandwiched UCNP-SP-PEG-MGN structure. Without magnetic field modulation, the coupling distance between UCNP and MGN is large due to the steric hindrance of SP, leading to a low energy transfer efficiency. In contrast, with a downward magnetic field, MGNs are pushed downward by stretching the flexible PEG linker, shortening the coupling distance between UCNPs and MGNs with an enhanced energy transfer efficiency. Under 980 nm laser excitation, the upconversion emission of UCNPs can then be efficiently absorbed by MGNs. By measuring the photoluminescence change, viral spike proteins can be detected. Our findings demonstrate this magnetic-responsive biosensor exhibits a linear relationship from 1 pg/mL to 1000 ng/mL with a 10-fold improved limit of detection (LOD) at 2.1 pg/mL under magnetic attraction compared with 20.6 pg/mL without magnetic attraction. Removal of the magnetic attraction reversibly restores the original signals. It is worth noting that the platform under +Mag still maintains the linear relationship and the removal of the magnetic attraction (−Mag) reversibly restores the original signals. The finite-difference time-domain (FDTD) optical simulation of MGNs approaching UCNPs on the substrate with cyclic distance change confirmed the distance-dependent energy transfer efficiency under magnetic attraction, which supported the experimental results. Our study not only proves a new concept of manipulating the coupling distance between donors and acceptors in the LRET biosensor, but also provides a promising strategy for magnetic-responsive UCNP-based LRET biosensor for other large-size biomolecule detection.

2. Materials and Methods

2.1 Materials

$Y(CH_3COO)_3 \cdot xH2O$ (99.9%), $Yb(CH_3COO)_3 \cdot 4H2O$ (99.9%), $Er(CH_3COO)_3 \cdot xH2O$ (99.9%), branched polyethyleneimine (BPEI, Mw~25,000), iron(III) chloride ($FeCl_3 \cdot 6H_2O$), hydroxylamine hydrochloride ($NH_2OH \cdot HCl$), and Gold(III) chloride trihydrate ($HAuCl_4$) were purchased from Sigma-Aldrich (St. Louis, MO, US). Iron(II) chloride tetrahydrate ($FeCl_2 \cdot 4H_2O$), succinic anhydride, and 4-Dimethylaminopyridine (DMAP) were purchased from Shanghai Aladdin Biochemical Technology Co., Ltd. (Shanghai, China). Trisodium citrate dihydrate was purchased from Alfa Aesar (Massachusetts, US). 3-Aminopropyltriethoxysilane (APTES), N,N-Dimethylformamide (99.9%, DMF), 3-[(Ethylimino)methylidene]amino-N,N-dimethylpropan-1-amine (EDC), Hydroxy succinimide (NHS), and albumin from bovine serum (BSA) were purchased from J&K Scientific LTD (Beijing, China). HS-PEG-NH_2 was purchased from Laysan Bio (Arab, US). Recombinant SARS-COV-2 B1.1.529 (Omicron) S1-S2 trimer Protein (40589-V08H26) and SARS-COV-2 Spike antibody (40150-D004) were purchased from Sino Biological Inc. (Beijing, China). Influenza A[A/Hong Kong/483/97/97(H5N1)] HA and MERS S1 protein were purchased from Acrobiosystems (Beijing, China). The SARS-COV-2 BA.2 lentivirus was kindly provided by Centre for Virology, Vaccinology and Therapeutics, the University of Hong Kong.

2.2 Synthesis and modification of $NaGdF_4$:Yb/Er upconversion nanoparticles

To synthesize UCNPs (Wang et al. 2014), 6 mL of oleic acid (OA) and 15 mL of 1-octadecene (OC) were added into a 50-mL flack (OA:OC=6:15) under room temperature. Then 0.8 mmol $Y(CH_3COO)_3$, 0.18mmol $Yb(CH_3COO)_3$, and 0.02 mmol $Er(CH_3COO)_3$ were added under stirring. The temperature was then raised to 150 °C and maintained for 40 minutes with the flask left uncovered. Afterward, the heating was turned off, and the flask was allowed to cool to room temperature. Following this, 2.5 mL of NaOH (1M in methanol) was mixed with 3.5 mL of NH_4F (1M in methanol) in a 15-mL centrifuge tube quickly and the resulting mixture was injected into the flack. The solution's temperature was elevated to 50 °C and held for 30 minutes. Subsequently, the temperature was increased to 100 °C and maintained for 20 minutes before connecting the flask to the pump and N_2. The temperature was then further raised to 280 °C, and the reaction proceeded under N_2 for 1.5 hours. Once again, the heating was turned off, and the mixture was cooled with stirring. The resulting mixture was transferred to a 15-mL tube, and twice the volume of ethanol was added. Centrifugation at 6000 rpm for 3 minutes followed by discarding the supernatant was performed. After that, 4 mL of cyclohexane and 8 mL of ethanol were added, and the mixture was vortexed and centrifuged at 6000 rpm for 3 minutes. This washing process was repeated, resulting in the obtained UCNPs.

To modify the UCNPs with amino groups (Guller et al. 2018), the prepared UCNPs were dispersed in ddH_2O under ultrasound at a concentration of 1 mg/mL. 160 μL of UCNPs were mixed with 500 μL of 15mg/mL BPEI (Mw=25,000, in chloroform). The

mixture was ultrasound for 5 min before stirring for 1.5 h with capped under room temperature. Afterward, the temperature was increased to 70 °C to evaporate the chloroform. Next, 1 mL of ddH_2O was added, followed by ultrasound treatment, and the mixture was stirred for 1 hour at room temperature. The UCNPs-PEI were separated by centrifugation (6000 rpm, 5 min) and washed with ddH_2O three times. Finally, the UCNPs-PEI were re-dispersed in 160 μL of ddH_2O to obtain a concentration of 1 mg/mL UCNPs-PEI.

2.3 Preparation of Fe_3O_4@Au-PEG-Abs Nps

1.79 g of $FeCl_3 \cdot 6H_2O$ and 1.10 g of $FeCl_2 \cdot 4H_2O$ were dissolved in 40 mL of ddH_2O. Subsequently, 5.5 mL of 28% $NH_3 \cdot H_2O$ was added under stirring. After 10 min, 4.4 g of trisodium citrate dihydrate was added, and the temperature was raised to 90 °C for 30 minutes. The Fe_3O_4 nanoparticles (Fe_3O_4 Nps) were washed with acetone twice and with ddH_2O once, and then separated using a magnet. The particles were freeze-dried to obtain the powdered product.

To coat the Fe_3O_4 Nps with Au layer, we employed the iterative hydroxylamine seeding method (Lin et al., 2019; Lyon et al., 2004). 0.2315 mg of Fe_3O_4 Nps were dispersed in 1 mL 0.1M tetramethylammonium hydroxide (TMAOH). And then, 0.1 mL of the Fe_3O_4/TMAOH solution was added to 100 mL of ddH_2O. Next, 3 mL 0.2 M trisodium citrate dihydrate was added, and the mixture was ultrasonicated for 5 minutes. After that, it was stirred for 10 minutes, and then 0.5 mL of 1wt% $HAuCl_4$ was slowly added. 10 seconds later, 0.2 mL of 0.2 M $NH_2OH \cdot HCl$ was quickly added, and the

reaction proceeded for 20 minutes. The above step was repeated four times. The Fe_3O_4 Nps with the gold coating (Fe_3O_4@Au Nps) were washed with ddH_2O three times (6000 rpm, 30 min) and collected using a magnet. Finally, the particles were freeze-dried to obtain the powdered product.

To link the S protein antibodies (Abs) with the Fe_3O_4@Au Nps, first, 10 μL of 100 mM 3-[(Ethylimino)methylidene]amino-N,N-dimethylpropan-1-amine (EDC), 10 μL of 100 mM N-Hydroxysuccinimide (NHS), and 20 μL of 1 mg/mL S protein Abs were mixed for 30 minutes. Subsequently, 1 μL of 2 mg/mL HS-PEG3400-NH_2 was added, and the mixture was stirred for 4 hours. An additional 100 μL of 0.01 M PBS was added, and an ultrafiltration centrifugal tube (10 kDa) was utilized to remove excess HS-PEG3400-COOH. Next, 100 μL of 1 mg/mL Fe_3O_4@Au Nps was added and the mixture was stirred for 4 hours at room temperature. The products were then separated using a magnet, and they were subsequently re-dispersed in 500 μL of 0.01 M PBS to form a solution with a concentration of 0.2 mg/mL.

2.4 Modification of glass slide

To modify the glass slide with the carboxyl group, the glass slide was initially immersed in 0.5 mL of a 37% HCl/methanol solution (v:v = 1:1) for 30 minutes. Then, it was washed with ddH_2O three times and then immersed in 98% H_2SO_4 for 30 minutes to activate the hydroxyl group. After that, the glass slide was washed with ddH_2O and ethanol three times. To further modify it with the amino group (Glass slide-NH_2), the activated glass slide was immersed in a solution of 1% 3-aminopropyl triethoxysilane

(APTES) in ethanol for 2 hours. It was then washed with ethanol twice and water twice. Glass slide-NH_2 was wash with dimethylformamide (DMF) once, then, immersed in a solution of 0.1 M succinic anhydride and 0.025 M 4-Dimethylaminopyridine (DMAP) in DMF. The reaction was left to proceed overnight, followed by washing with DMF once and ddH_2O twice to obtain the glass slide with carboxyl group modification (Glass slide-COOH). To modify the glass slide with UCNPs, the Glass slide-COOH was incubated with 500 μL of 50 mM EDC/NHS for 30 minutes. It was then quickly dried using N_2, and 20 μL of a 0.5 mg/mL UCNPs-PEI solution was evenly spread on the surface and left to react overnight, resulting in the creation of the Glass slide-UCNPs. Finally, for the modification of S protein Abs, 100 mM EDC and NHS solutions were prepared using 0.01 M PBS. 15 μL of each solution were mixed, and 10 μL of 100 μg/mL S protein Abs were added, followed by a 30-minute incubation at room temperature. This mixture was then dropped onto the Glass slide-UCNP and left to incubate for 4 hours. After that, 1 mg/mL of bovine serum albumin (BSA) was used to block the surface for 30 min. The glass slide was subsequently dried using N_2 and stored at 4 °C.

2.5 Detection of SARS-CoV-2 S protein

The Glass slide-UCNPs was initially incubated with S protein at various concentrations in 0.1 M PBS (0, 0.001, 0.01, 0.1, 1, 10, 100, and 1000 ng/mL) for 30 minutes. Subsequently, it was carefully washed twice with 0.1 M PBS. Next, it was incubated with 200 μg/mL of Fe_3O_4@Au-PEG-Abs Nps for 30 min and then carefully

washed twice with 0.1 M PBS. An external magnetic field was applied using a magnet for 10 minutes before measuring the photoluminescence spectra under 980 nm laser irradiation. The relative fluorescence signal was calculated as follows:

$$Relative\ Fluorescence\ Signal = 1 - \frac{F}{F_0} \quad (1)$$

F represents the fluorescence intensity of Glass slide-UCNPs after capturing the S protein and adding Fe_3O_4@Au-PEG-Abs Nps, and F_0 represents the fluorescence intensity before capturing the S protein. The LOD of the platform was calculated based on the signal of control group plus three times the standard deviation.

2.6 The specificity and stability of the detection platform

For the specificity evaluation, we measured the relative fluorescence signal of 1000 ng/mL MERS S1, Influenzas A, and SARS-CoV-2 S protein in 0.1 M PBS. The proteins were first incubated with the Glass slide-UCNPs and the Fe_3O_4@Au-PEG-Abs Nps, then magnetic modulation was applied before testing the fluorescence signal. For the stability evaluation, we firstly measured the photoluminescence spectra of 0.1 mg/mL UCNPs-PEI in ddH_2O, 1x PBS, Tris-HCl (pH=8.0), lysis buffer, swab, and blood plasma to assess the stability of the UCNPs-PEI. Next, we measured the relative fluorescence signal while adding 1000 ng/mL S protein in ddH_2O, 1x PBS, lysis buffer, swab, and blood plasma to the Glass slide-UCNPs with the Fe_3O_4@Au-PEG-Abs Nps added.

2.7 Finite-Difference Time-Domain (FDTD) Simulation

To conduct the LRET calculation, the spectra overlap $\int I_d(\lambda)\varepsilon_a(\lambda)\lambda^4 d\lambda)$ is extracted from the normalized experiental UV absborance spectra of F Fe_3O_4@Au Nps and UCNPs. The extracted spectra overlap determines the Förster distance (R0) of the donor pair system, where $Ro = 0.021(k^2 n^{-4}\Phi_d \int I_d(\lambda)\varepsilon_a(\lambda)\lambda^4 d\lambda)^{-6}$, k^2 is orientation factor which is typically 2/3, Φ_d is quantum efficiency of the UCNP which is 3% (Jones et al. 2021) is our calculation, n is the refraction index of the medium surrounding ($n_{water} = 1.55$) water is the refraction index of the surrounding medium. After obtaining the Ro, the LRET efficiency is calculated by:

$$E = \frac{1}{1 + (\frac{r}{Ro})^6} \quad (2)$$

where r is the distance between the Fe_3O_4@Au Nps and UCNPs.

2.8 Statistical Analysis

For each concentration of S protein, we tested the spectrum of 5 random points on the surface of the glass slide, and three Glass slide-UCNPs were used for the detection (n=3). Statistical analysis of pairwise comparison was determined by one-way ANOVA.

3. Results and discussion

3.1 Synthesis and characterization of Fe_3O_4@Au-PEG-Abs Nps and UCNPs

Firstly, we synthesized Fe_3O_4 magnetic nanoparticles (Fe_3O_4 Nps) with the size of 10.1 ± 3.0 nm using the coprecipitation method (Fig. 1A). The gold shell was then

coated by reducing $HAuCl_4$ on the surface of the Fe_3O_4 Nps to form Fe_3O_4@Au nanoparticles (MGN) (Fig. S1). After gold shell coating, the size of Fe_3O_4@Au Nps increased to 30.5 ± 5.6 nm in the TEM image (Fig. 1B), and the hydrodynamic size distribution analysis also showed a significant increase of size after Au shell coating (Fig. S2A). The zeta potential of also changed from -44.8 ± 3.1 mV of Fe_3O_4 Nps to -18.6 ± 2.3 mV of Fe_3O_4@Au Nps (Fig. S2B). Moreover, the co-localization of the Au and Fe element in the element mapping image of Fe_3O_4@Au Nps also confirmed the successful coating of gold shell on the Fe_3O_4 Nps (Fig. 1C). Antibodies were then linked to Fe_3O_4@Au Nps via a flexible PEG linker (HS-PEG-NH_2) to form Abs-PEG-MGN Nps (Fig. S1). To realize it, the anti-S protein antibodies were firstly modified with the PEG linker and the UV-vis spectrum of HS-PEG-Abs confirmed this modification with the characteristic absorption peak of proteins at 280 nm (Fig. S3). Then, the HS-PEG-Abs were further conjugated on the gold shell of Fe_3O_4@Au Nps through the thiol–gold interactions (Cruz et al. 2019; Wang et al. 2013). The UV-vis spectrum of Abs-PEG-MGN Nps showed the characteristic peaks at 280 nm and 540 nm for proteins and gold shell, respectively (Fig. 1D). The magnetic property of Abs-PEG-MGN Nps was also confirmed by the vibrating sample magnetometer (VSM) spectrum (Fig. 1E).

We synthesized the $NaYF_4$:Yb/Tm upconversion nanoparticles (UCNPs) by the hydrothermal method and obtained oleic acid capped UCNPs (UCNPs-OA) with an average size around 80 nm (Fig. 1F). Polyethyleneimine (PEI) was then used for ligand exchange to obtain PEI-capped UCNPs (UCNPs-PEI) with good water dispersity (Fig. 1G). After ligand replacement with PEI, the zeta-potential of UCNPs was changed from

negative to positive since the PEI group is highly polycationic (Fig. 1H), and the hydrodynamic size distribution peak of UCNPs-PEI were slightly increased (Fig. S4).

3.2 Establishment of UCNP-based LRET biosensor for S protein detection without magnetic modulation

The UCNP-based LRET biosensor for S protein detection was then established on a glass substrate (Fig. S5). Briefly, a glass substrate was first modified with carboxyl groups via silane chemistry. The UCNPs-PEI were then conjugated on the surface of carboxyl groups-functionalized glass slide via EDC/NHS chemistry. A uniform distribution of UCNPs on the glass slide was observed (Fig. 2A). After washing and deactivation of the excessive carboxyl groups on the glass slide, antibodies specific for S protein were then conjugated on the UCNPs of the glass slide via the binding between carboxyl groups on antibodies and amine groups on UCNPs-PEI. Finally, BSA was coated on the sensor surface to present non-specific binding. It was observed that the water contact angle of the glass slide was firstly decreased after modification with carboxyl groups via silane and then increased after modification with antibodies (Fig. 2B and Fig. S6). Under 980 nm irradiation, this UCNP-based LRET biosensor showed a uniform green fluorescence and red fluorescence on the substrate (Fig. 2C). Generally, under the 980 nm laser excitation, the $^2F_{7/2} \rightarrow {}^2F_{7/2}$ electronic transitions appear in Yb^{3+}. The energy can transfer to Er^{3+}, resulting in the emission mainly at 541 nm (green), and 657 nm (red), which corresponds to the transition of $^4S_{3/2} \rightarrow {}^4I_{15/2}$, and $^4F_{9/2} \rightarrow {}^4I_{15/2}$ (Fig. S7) (Dong et al. 2015). The photoluminescence spectrum of UCNPs at 541 nm

and the UV-vis spectrum of Fe_3O_4@Au NPs showed good overlap, which laid a good foundation for the proposed UCNP-based LRET biosensor (Fig. 2D).

The established UCNP-based LRET biosensors were then firstly tested for S protein detection without magnetic modulation. In the presence of target S proteins, S proteins were captured by antibody-functionalized UCNPs on the glass substrate and then labelled with Abs-PEG-MGN Nps to form sandwiched structure. The unbound Abs-PEG-MGN Nps were then washed away. Various concentrations of S proteins from 1 pg/mL to 1000 ng/mL were then added for incubation about 20 minutes. After washing, excessive Abs-PEG-MGN Nps with a concentration of 200 μg/mL were then added for incubation for another 20 minutes. A high concentration of Abs-PEG-Fe_3O_4@Au Nps was used to ensure that S proteins were fully labeled. Unbound Abs-PEG-Fe_3O_4@Au Nps were then washed away for fluorescence measurement. The conjunction of Abs-PEG-MGN Nps with UCNPs were confirmed by TEM imaging (Fig. 2E). Moreover, the appearance of Au4f peak in the XPS spectrum also confirmed the conjugation of Abs-PEG-MGN on the UCNP-modified glass substrates (Fig. S8). A S protein concentration-dependent fluorescence intensity decrease at 514 nm was observed in the fluorescence spectrum and confocal fluoresce images (Fig. 2F). The confocal images under 980 nm irradiation also showed the fluorescence signal change when adding S protein with different concentrations (Figure S9). A linear detection range ($y = 0.1111x + 0.3622$, $R^2 = 0.9229$) from 0.1 ng/mL to 1000 ng/mL was observed between the relative fluorescence signal change and the logarithmic concentration of S protein, and a limit of detection (LOD) of 20.6 pg/mL was calculated as the signal of

control group plus 3 times of standard derivation (Fig. 2G, 2H).

3.3 S protein detection with magnetic modulation

We then explored the effect of magnetic modulation on the performance of the magnetic-responsive UCNP-based LRET biosensor. Under magnetic modulation, Abs-PEG-Fe_3O_4@Au Nps with flexible PEG linker are attracted downward, enhancing energy transfer between donors and acceptors due to the shortened coupling distance (Fig. 3A). Generally, the magnetic response of MGNs is determined by two factors including the size of Fe_3O_4 magnetic core and the magnetic field strength. The original distance between Abs-PEG-MGN Nps and UCNP upon switching the S protein can be calculated by the summation of two sandwiching S protein antibodies (~10 nm x 2) (Kamogawa et al., 2012) and S protein (~20 nm) (Ke et al., 2020). At the resting state, the PEG linker (MW=3400) is highly coiled (Liu et al., 2014), where the MGNs mainly stay on top of the S protein. Thus, the estimated initial separation distance is 40 nm. Note that the fully stretched PEG linker has ~21.5 nm (Ma et al., 2014) and the size of MGN is ~30.5 nm, which together are longer than 50 nm for the separation distance (Figure S10).

Magnetic response of MGNs is critical for rapid and sensitive detection of this LRET biosensor. Generally, magnetic response of MGNs is determined by two factors including the size of Fe_3O_4 magnetic core and the magnetic field strength. MGNs with larger size of Fe_3O_4 core possesses a higher saturation magnetization, enhancing the responsiveness of MGNs to the external magnetic field (Kolhatkar et al., 2013).

However, larger size of NPs will also increase the drag force in the fluid solution to slow down the magnetic response. Therefore, in our experimental design, we proposed to use various magnetic fields to optimize the magnetic response of MGNs with a fixed size of Fe_3O_4 core ~10 nm and a gold coating of 10 nm. Here, we firstly used one magnet (measured at 198 mT), two stacked magnets (measured at 320mT) and three stacked magnets (measured at 486 mT) to represent different magnetic field strengths and adhere them to the bottom surface of the glass substrates to explore how quickly the free MGNs in the solution can be attracted to the bottom of the glass substrates. The unattracted MGNs in the solution after magnetic attraction were measured by UV-Vis spectroscopy at 541 nm. As shown in Figure S11, two magnets and three magnets generally had quicker response of MGNs compared with one magnet. Almost all the MGNs in the solution were attracted to the bottom within 5 minutes and there is no obvious difference for two magnets and three magnets for attracting MGNs especially after 5 minutes. As a demonstration, S protein with a concentration of 0.1 ng/mL with a PEG linker of 3400 MW was used to compare the upconversion fluorescence signal without or with magnetic modulation of 1 magnet, 2 stacked magnets and 3 stacked magnets. It was observed that the upconversion fluorescence signal without magnetic attraction for 0.1 ng/mL of S protein only decreased a little compared with the control group. In contrast, the upconversion fluorescence signal showed an obvious decrease with magnetic modulation (Fig. 3B). Moreover, it was observed that stronger magnetic field strength with 2 stacked magnets could further improve the quenching effect, but there is no obvious difference for two stacked magnets and three stacked magnets.

Therefore, the magnetic field strength as 320 mT generated by 2 stacked magnets with optimized magnetic response were chosen for our following sensing experiments. This demonstrated that magnetic modulation could improve the sensitivity of this UCNP-based biosensor by enhancing the energy transfer.

We then further explored the effect of the length of the PEG linkers (MW=400, 3400 and 5000) on the energy quenching efficiency (Fig. 3C). It was observed that there was no significant increase of energy quenching efficiency for the PEG linker (MW=400). When the PEG linker length increased to MW of 3400, the quenching efficiency showed a significant increase. However, the further increase of the length to MW of 5000 did not further improve the quenching efficiency. Generally, if the PEG linker is too short, the magnetic attraction can not efficiently push the Abs-PEG-MGN Nps close to the UCNPs. If the length of the PEG linker reaches a certain level, the magnetic attraction can stretch the PEG linker, bringing the Abs-PEG-MGN Nps very close to the surface of UCNPs, while longer PEG linkers beyond this level do not bring more benefits. Therefore, the Fe_3O_4@Au-PEG3400-Abs NPs were chosen as the acceptor for the detection platform in the following experiments. We then explored the LOD and linear detection range of this biosensor under magnetic modulation. It was observed that the upconversion fluorescence signal also decreased with the increase of S protein concentrations (Fig. 3D). The LOD was improved to 2.1 pg/mL with a linear detection range ($y = 0.1250\ x + 0.4874$, $R^2 = 0.9887$) from 0.001 ng/mL to 1000 ng/mL between the relative fluorescence signal change and the logarithmic concentration of S protein (Fig. 3E and 3F). Moreover, we measured the relative fluorescence signal

change while applying the external magnetic field (Fig. S12). This LRET biosensor showed a quick response with the external magnetic field. The relative fluorescence signal increased with the applied magnetic field in the first five minutes and then remained stable. The total detection time of this LRET biosensor was within 1 hour including 40 minutes incubation time, 5 minutes of magnetic attraction time and time needed for other steps such as sample loading and measurement.

3.4 Specificity and reliability testing

We then tested the specificity of this biosensor with two non-specific proteins of MERS S1 and Influenza A HA with a concentration of 1000 ng/mL (Fig. 4A). The results showed that there was no obvious fluorescence signal change for groups of MERS S1 and Influenza A HA compared with the control group. In contrast, the group of SARS-CoV-2 S protein showed an obvious signal change. The above result demonstrated the specificity of our biosensor for SARS-CoV-2 S protein detection. We then accessed the stability of photoluminescence of UCNPs-PEI in various media. As shown in Fig. S14, UCNPs-PEI showed stable photoluminescence in ddH_2O, normal saline, PBS, RIPA lysis buffer, Tris-HCl buffer, virus preservation solution (VPS), swab, and serum. We then tested the performance of this biosensor for S protein of a concentration of 1000 ng/mL in various media including ddH_2O, normal saline, PBS, RIPA lysis buffer, VPS, swab, and serum. All the groups showed similar signal change compared with the control group, which demonstrated that our biosensor could detect S protein stably in different media (Fig. 4B). Moreover, the sensitivity and linear

detection range of this biosensor in swab and serum were tested. This biosensor with magnetic modulation showed a LOD of 17 pg/mL in swab with a linear detection range (y =0.1072 x+0.3947, R^2=0.9500) (Fig. 4C, 4D and 4E), and a LOD of 4.2 pg/mL in serum with a linear detection range (y =0.1214 x+0.4586, R^2=0.9859) (Fig. 4F, 4G and 4H). The above results demonstrated the good reliability of this biosensor in various media. To further demonstrate the clinical applicability of our sensor, we conducted a test with the SARS-CoV-2 lentivirus, utilizing a concentration of 5×10^2 pfu/mL in lysis buffer. As shown in Figure S13, the LRET sensor without magnetic modulation did not show significant difference with the control group. In contrast, the LRET sensor with magnetic modulation showed significant difference compared with the control group, which demonstrated the capability for clinical sample detection. The viral load on the clinical sample was reported distributed according to log-normal distribution with the mean of 9.9×10^8 virions/mL (Yang et al., 2021) and 10^4-10^5 PFU/mL is a common viral load level (Lin et al., 2022), which is much higher than our platform detection limit.

3.5 Mechanism of magnetic modulation-enhanced LRET biosensor

To further explore the mechanism of magnetic modulation-enhanced LRET biosensor, we compared the relative signal change for a serious of concentrations of S proteins before and after magnetic modulation. The results showed that the sensing signals were improved for all the concentration groups (Fig. 5A). Moreover, we demonstrated a cyclic switching between +Mag and −Mag to manipulate LRET signal

enhancement reversibly in 3 cycles (Fig. 5B). Each +Mag cycle maintained a highly similar enhanced LRET signal, which demonstrated the stability and reversibility of this magnetic-responsive LRET sensing platform for protein detection. We then further performed finite-difference time-domain (FDTD) simulation with cyclic distance change to explore the effect of magnetic-modulation controlled distance on the quenching efficiency. In our platform, the external magnetic field controls the distance between the UCNPs and acceptors. Without magnetic modulation, the distance between UCNPs and acceptors for protein detection is large due to the large steric hindrance of proteins. The SARS-CoV-2 S protein is reported to be around 20 nm (Ke et al. 2020), which generates large steric hindrance between the donors and the acceptors. With magnetic modulation, the distance between UCNPs and acceptors is shortened by stretching the flexible PEG liner, leading to an enhanced quenching efficiency (Fig. 5C). Based on the simulated distance-dependent quenching efficiency of this UCNP-based LRET biosensor (Fig. 5D), the simulated quenching efficiency change under magnetic modulation cycling was shown in Fig. 5E, which matched well with the experimental result in Fig. 5B. Compared with the current FRET protein sensors, this unique design of magnetic-responsive LRET sensor could overcome the large steric hindrance of proteins and significantly improve the sensitivity for protein detection (Table S1).

4. Conclusion

In this study, we successfully established a magnetic-responsive LRET-based upconversion nanoprobe system for SARS-CoV-2 S protein detection. The special

design of the acceptor with a flexible PEG linker could allow the magnetic control of the coupling distance between UCNPs and acceptors to overcome the large steric hindrance of proteins under the magnetic field. Therefore, the LRET effect can be enhanced and result in higher quenching efficiency. Our platform is demonstrated to have a low LOD for S protein detection, rapid detection, good specificity and good reliability, indicating excellent potential for clinical application. This kind of magnetic-response LRET sensor is not only limited to detection of SARS-CoV-2 S protein, but also easily adapted for other large biomolecules detection.

CRediT authorship contribution statement

J.C. designed and performed experiments, analyzed the data, and wrote the manuscript. W.K.H.H. contributed to the finite-difference time-domain (FDTD) simulation. B.Y contributed to the preparation of glass slide modification. Q.Z. contributed to the confocal images. C.L., J.Y and Y.H contributed to the synthesis of UCNPs. J.H., C.Y. and Y.Z. contributed to editing the paper. W.S.H.D. and M.Y. conceived the idea, edited the paper, and supervised the whole study. W.S.H.D. and M.Y. provided funding support. All authors reviewed and approved the paper.

Declaration of Competing Interest

The authors report no declarations of interest.

Acknowledgments

This work was supported by the Research Grants Council (RGC) Collaborative Research Fund (C5110-20G), the Shenzhen-Hong Kong-Macao Science and Technology Plan Project (Category C, SGDX2020110309260000), the Research Grants Council (RGC) of Hong Kong General Research Fund (PolyU 15216622, 15217621 and 15214619), the Guangdong-Hong Kong Technology Cooperation Funding Scheme (GHP/032/20SZ and SGDX20201103095404018), the Hong Kong Polytechnic University Shenzhen Institute Bai Cheng Bai Yuan Fund (I2022A002), and the Hong Kong Polytechnic University Internal Fund (1-ZVVQ, 1-CD6J and 1-CD8M). W.S.H.D. would like to acknowledge the start-up funding (1-ZVRY) from the Department of Biomedical Engineering and Start-up Fund for RAPs under the Strategic Hiring Scheme (1-BD8Q), the Hong Kong Polytechnic University (PolyU, University Grant Council), and PolyU Projects of RISports (1-CD5P) for supporting this work. This work was also supported by the University Research Facility in Life Sciences of the Hong Kong Polytechnic University.

References

Callaway, E. Why a highly mutated coronavirus variant has scientists on alert. Nature. 2023 Aug 21. doi: 10.1038/d41586-023-02656-9. Epub ahead of print.

Callaway, E. Why a highly mutated coronavirus variant has scientists on alert. Nature. 2023 Aug 21. doi: 10.1038/d41586-023-02656-9. Epub ahead of print.

Choi, J.H., Ha, T., Shin, M., Lee, S.N., Choi, J.W., 2021. Nanomaterial-based

fluorescence resonance energy transfer (FRET) and metal-enhanced fluorescence (MEF) to detect nucleic acid in cancer diagnosis. Biomedicines, 9(8), 928.

Cruz, E., Kayser, V., 2019. synthesis and enhanced cellular uptake in vitro of anti-HER2 multifunctional gold nanoparticles. Cancers (Basel), 11(6), 870.

Dong, H., Sun, L.D., Yan, C.H., 2015. Energy transfer in lanthanide upconversion studies for extended optical applications. Chem Soc Rev, 44(6), 1608-1634.

Guller, A.E., Nadort, A., Generalova, A.N., Khaydukov, E.V., Nechaev, A.V., Kornienko, I.A., Petersen, E.V., Liang, L., Shekhter, A.B., Qian, Y., Goldys, E.M., Zvyagin, A.V., 2018. Rational surface design of upconversion nanoparticles with polyethylenimine coating for biomedical applications: better safe than brighter? ACS Biomater Sci Eng, 4(9), 3143-3153.

He, J ., Zhu, S.Y., Zhou, J.W., Jiang, W.J., Yin, L.L., Su, L., Zhang, X.L., Chen, Q., Li, X.P., 2023. Rapid detection of SARS-CoV-2: The gradual boom of lateral flow immunoassay, Front. Bioeng. Biotechnol., 10, 1090281.

Jones, C.M.S., Gakamsky, A., Marques-Hueso, J., 2021. The upconversion quantum yield (UCQY): a review to standardize the measurement methodology, improve comparability, and define efficiency standards. Sci Technol Adv Mater, 22(1), 810-848.

Kamogawa, M., Shimanuki, J., Azuma, T., Murakami, A., Ishiguro, T., 2012. Transmission Electron Microscopy Observation of Antibody. Procedia Engineering, 36, 150-153.

Ke, Z., Oton, J., Qu, K., Cortese, M., Zila, V., McKeane, L., Nakane, T., Zivanov, J., Neufeldt, C.J., Cerikan, B., Lu, J.M., Peukes, J., Xiong, X., Krausslich, H.G.,

Scheres, S.H.W., Bartenschlager, R., Briggs, J.A.G., 2020. Structures and distributions of SARS-CoV-2 spike proteins on intact virions. Nature, 588(7838), 498-502.

Kevadiya, B.D., Machhi, J., Herskovitz, J., Oleynikov, M.D., Blomberg, W.R., Bajwa, N., Soni, D., Das, S., Hasan, M., Patel, M., Senan, A.M., Gorantla, S., McMillan, J., Edagwa, B., Eisenberg, R., Gurumurthy, C.B., Reid, S.P.M., Punyadeera, C., Chang, L., Gendelman, H.E., 2021. Diagnostics for SARS-CoV-2 infections. Nat Mater, 20(5), 593-605.

Kim, G.B., Kim, Y.P., 2012. Analysis of protease activity using quantum dots and resonance energy transfer. Theranostics, 2(2), 127-138.

Li, D., Liu, Y., Yu, S., Zhang, D., Wang, X., Zhong, H., He, K., Wang, Y., Wu, Y.X., 2021. A two-photon fluorescence silica nanoparticle-based FRET nanoprobe platform for effective ratiometric bioimaging of intracellular endogenous adenosine triphosphate. Analyst, 146(15), 4945-4953.

Lin, C.-W., Chen, J.-M., Lin, Y.-J., Chao, L.-W., Wei, S.-Y., Wu, C.-H., Jeng, C.-C., Wang, L.-M., Chen, K.-L., 2019. Magneto-optical characteristics of streptavidin-coated Fe_3O_4@Au Core-Shell nanoparticles for potential applications on biomedical assays. Scientific Reports, 9(1), 16466.

Liu, L., Rong, Q., Ke, G., Zhang, M., Li, J., Li, Y., Liu, Y., Chen, M., Zhang, X.B., 2019. Efficient and reliable microRNA imaging in living cells via a FRET-based localized hairpin-DNA cascade amplifier. Anal Chem, 91(5), 3675-3680.

Liu, L., He, F., Yu, Y., Wang, Y., 2020b. Application of FRET biosensors in

mechanobiology and mechanopharmacological screening. Front Bioeng Biotechnol, 8, 595497.

Liu, R., Han, H., Liu, F., Lv, Z., Wu, K., Liu, Y., Feng, Y., Zhu, C., 2020a. Positive rate of RT-PCR detection of SARS-CoV-2 infection in 4880 cases from one hospital in Wuhan, China, from Jan to Feb 2020. Clin Chim Acta, 505, 172-175.

Lin, Y.C., Malott, R.J., Ward, L., Kiplagat, L., Pabbaraju, K., Gill, K., Berenger, B.M., Hu, J., Fonseca, K., Noyce, R.S., Louie, T., Evans, D.H., Conly, J.M., 2022. Detection and quantification of infectious severe acute respiratory coronavirus-2 in diverse clinical and environmental samples. Sci Rep, 12(1), 5418.

Liu, Y., Medda, R., Liu, Z., Galior, K., Yehl, K., Spatz, J.P., Cavalcanti-Adam, E.A., Salaita, K., 2014. Nanoparticle Tension Probes Patterned at the Nanoscale: Impact of Integrin Clustering on Force Transmission. Nano Letters, 14(10), 5539-5546.

Lyon, J.L., Fleming, D.A., Stone, M.B., Schiffer, P., Williams, M.E., 2004. Synthesis of Fe oxide core/Au shell nanoparticles by iterative hydroxylamine seeding. Nano Letters, 4(4), 719-723.

Ma, Z., LeBard, D.N., Loverde, S.M., Sharp, K.A., Klein, M.L., Discher, D.E., Finkel, T.H., 2014. TCR triggering by pMHC ligands tethered on surfaces via poly(ethylene glycol) depends on polymer length. PLoS One, 9(11), e112292.

Mahmoudinobar, F., Britton, D., Montclare, J.K., 2021. Protein-based lateral flow assays for COVID-19 detection. Protein Eng Des Sel, 34.

Mu, J., Liu, F., Rajab, M.S., Shi, M., Li, S., Goh, C., Lu, L., Xu, Q.H., Liu, B., Ng, L.G., Xing, B., 2014. A small-molecule FRET reporter for the real-time visualization of cell-surface proteolytic enzyme functions. Angew Chem Int Ed Engl, 53(52), 14357-14362.

Jun, J.V., Chenoweth, D.M., Petersson, E.J., 2020. Rational design of small molecule fluorescent probes for biological applications, Organic & Biomoleuclar Chemistry, 18(30), 5747-5763.

Sapsford, K.E., Berti, L., Medintz, I.L., 2006. Materials for fluorescence resonance energy transfer analysis: beyond traditional donor-acceptor combinations. Angew Chem Int Ed Engl, 45(28), 4562-4589.

Selvin, P.R., 2000. The renaissance of fluorescence resonance energy transfer. Nat Struct Biol, 7(9), 730-734.

Song, M.L., Wong, M.C., Li, L.H., Guo, F., Liu, Y., Ma, Y.J., Lao, X.Y., Wang, P., Chen, H.L., Yang, M., Hao, J.H., 2023. Rapid point-of-care detection of SARS-CoV-2 RNA with smartphone-based upconversion luminescence diagnostics, Biosensors & Bioelectronics, 222, 114987.

Tsang, M.K., Ye, W., Wang, G., Li, J., Yang, M., Hao, J., 2016. Ultrasensitive detection of ebola virus oligonucleotide based on upconversion nanoprobe/nanoporous membrane system. ACS Nano, 10(1), 598-605.

Wang, C., Li, X., Zhang, F., 2016. Bioapplications and biotechnologies of upconversion nanoparticle-based nanosensors. Analyst, 141(12), 3601-3620.

Wang, F., Deng, R., Liu, X., 2014. Preparation of core-shell $NaGdF_4$ nanoparticles doped with luminescent lanthanide ions to be used as upconversion-based probes. Nature protocols, 9(7), 1634-1644.

Wang, S., Zhang, L., Kan, A., Xu, X., Zhang, N., Jiang, W., 2021. MnO(2) nanosheet-mediated target-binding-induced FRET strategy for multiplexed microRNAs

detection and imaging in living cells. Talanta, 226, 122202

Wang, W., Wei, Q.Q., Wang, J., Wang, B.C., Zhang, S.H., Yuan, Z., 2013. Role of thiol-containing polyethylene glycol (thiol-PEG) in the modification process of gold nanoparticles (AuNPs): stabilizer or coagulant? J Colloid Interface Sci, 404, 223-229.

Yang, Q., Saldi, T.K., Gonzales, P.K., Lasda, E., Decker, C.J., Tat, K.L., Fink, M.R., Hager, C.R., Davis, J.C., Ozeroff, C.D., Muhlrad, D., Clark, S.K., Fattor, W.T., Meyerson, N.R., Paige, C.L., Gilchrist, A.R., Barbachano-Guerrero, A., Worden-Sapper, E.R., Wu, S.S., Brisson, G.R., McQueen, M.B., Dowell, R.D., Leinwand, L., Parker, R., Sawyer, S.L., 2021. Just 2% of SARS-CoV-2−positive individuals carry 90% of the virus circulating in communities. Proceedings of the National Academy of Sciences, 118(21), e2104547118.

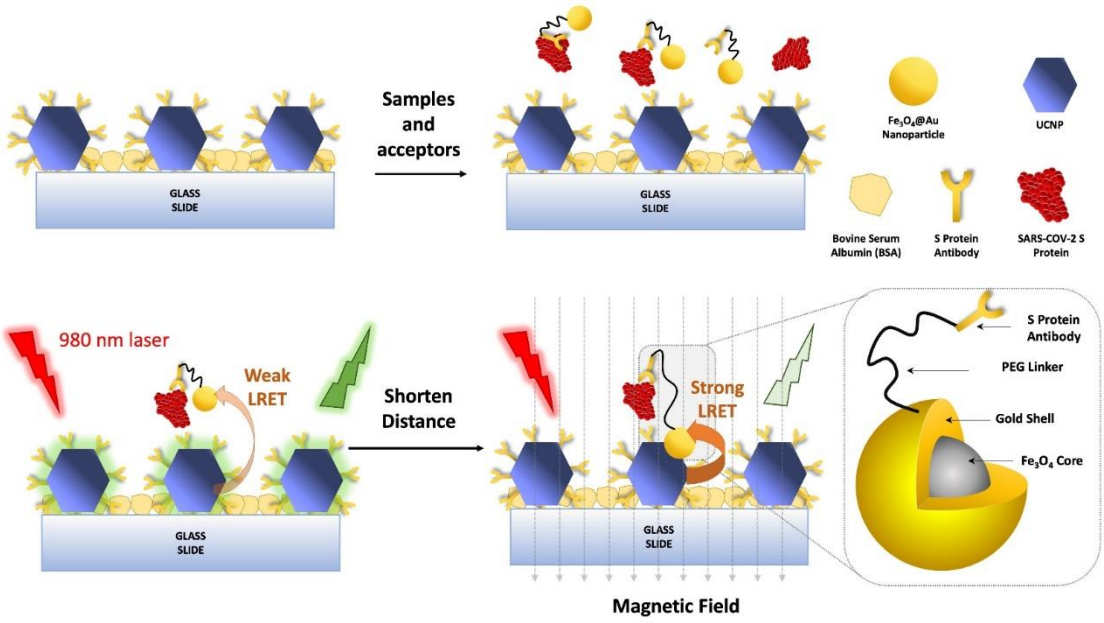

Scheme 1 Upconversion luminescence resonance energy transfer (LRET) biosensor for ultrasensitive detection of SARS-CoV-2 spike protein.

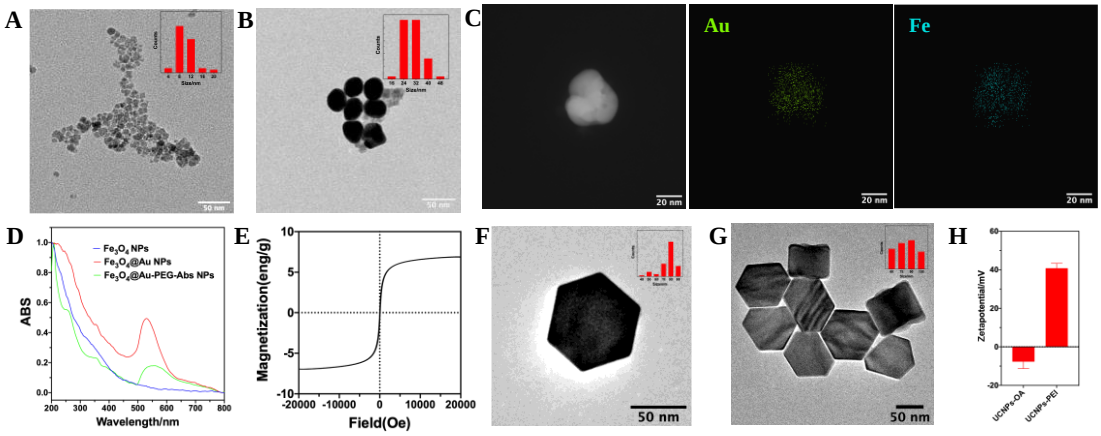

Fig. 1 Synthesis and characterization of Fe_3O_4@Au-PEG-Abs Nps and UCNPs. (A) TEM images of Fe_3O_4 Nps, insert was the size distribution of the nanoparticles. (B) TEM images of Fe_3O_4@Au Nps, insert was the size distribution of the nanoparticles. (C) Dark-field TEM image and corresponding area-elemental mapping of Fe_3O_4@Au Nps. (D) UV-vis spectrum of Fe_3O_4 Nps, Fe_3O_4@Au Nps, and Fe_3O_4@Au-PEG-Abs Nps. (E) Hysteresis loop of Fe_3O_4@Au Nps. (F) TEM images of UCNPs-OA, insert was the size distribution of the nanoparticles. (G) TEM images of UCNPs-PEI, insert was the size distribution of the nanoparticles. (H) ξ-potential of UCNPs-OA and UCNPs-PEI.

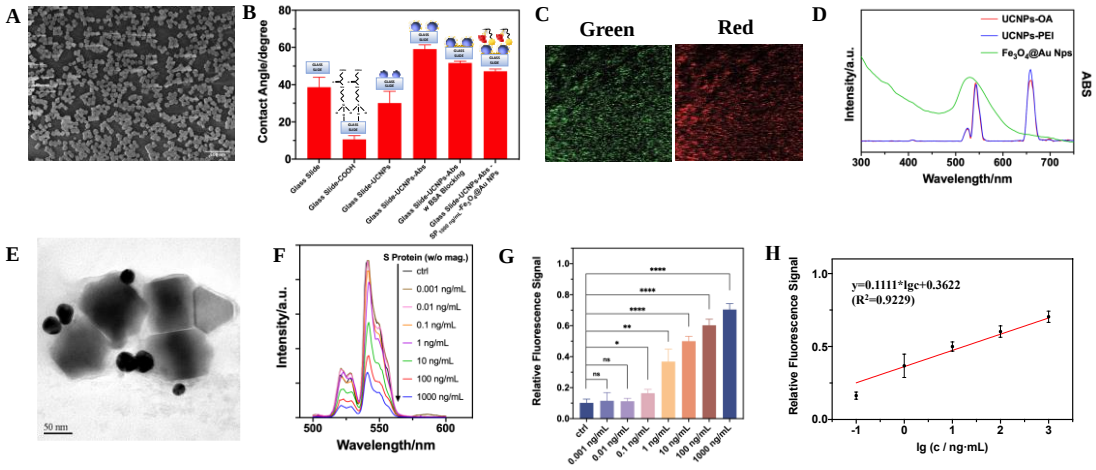

Fig. 2 Establishment of UCNP-based LRET biosensor for S protein detection. (A) SEM image of glass slide with UCNPs modification. (B) Contact angle of H_2O on glass slide and with different modification. (C) Confocal image of glass slide with UCNPs modification under the 980 nm laser irradiation. (D) Up-conversion photoluminescence spectrum of UCNPs-OA, UCNPs-PEI and UV-vis spectrum of Fe_3O_4@Au Nps. (E) TEM image of conjunction of Abs-PEG-MGN Nps with UCNPs. (F) Up-conversion photoluminescence spectrum of Glass Slide-UCNPs quenched by S protein with different concentration without magnetic field. (G) Relative fluorescence signal of S protein with different concentration without the magnetic field. No significance (ns): $P > 0.05$, $*P \leq 0.05$, $**P \leq 0.01$, $***P \leq 0.001$, $****P \leq 0.0001$. (H) Linear fit between the relative fluorescence signal and the lg concentration of S protein (from 0.1 ng/mL to 1000 ng/mL).

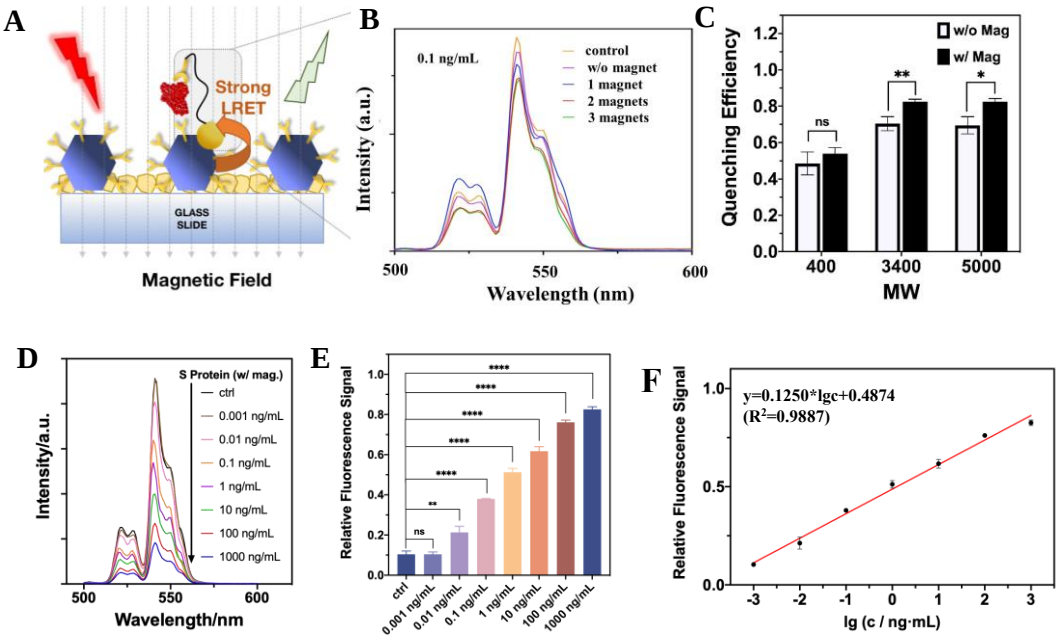

Fig. 3 Evaluation of the performance of the UCNP-based LRET biosensor for S protein detection under the magnetic modulation. (A) Illustration of the shortened distance between the UCNPs and the Fe_3O_4@Au Nps under the magnetic field via the flexible PEG linker. (B) The fluorescence spectra of various groups without adding S protein (ctrl), without magnetic modulation, with 1 magnet, 2 magnets and 3 magnets when adding 0.1 ng/mL S protein. (C) The comparation of quenching efficiency using the acceptor with different length of the PEG linker (MW=400, 3400, and 5000). (D) Up-conversion photoluminescence spectrum of Glass Slide-UCNPs quenched by S protein with different concentration under the magnetic modulation. (E) Relative fluorescence signal of S protein with different concentration under the magnetic modulation. No significance (ns): $P > 0.05$, $*P \leq 0.05$, $**P \leq 0.01$, $***P \leq 0.001$, $****P \leq 0.0001$. (F) Linear fit between the relative fluorescence signal and the lg concentration of S protein (from 0.01 ng/mL to 1000 ng/mL).

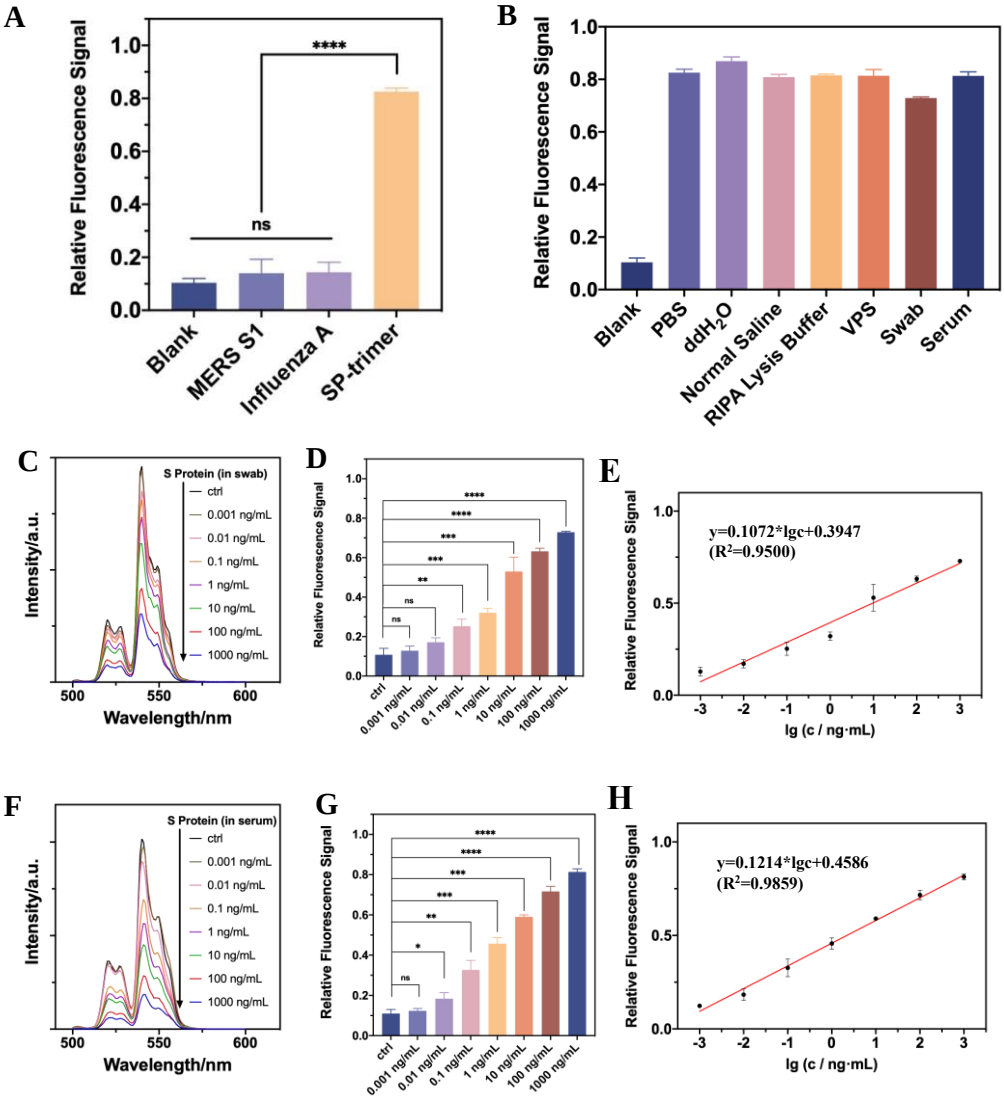

Fig. 4 Selectivity and stability of the UCNP-based LRET biosensor. (A) Relative fluorescence signal of the MESR S1, Influenza A, and SARS-Cov-2 S protein. (B) Relative fluorescence signal while detecting the SARS-Cov-2 S protein in PBS, ddH_2O, normal saline, RIPA lysis buffer, virus preservation solution (VPS), swab, and serum. Up-conversion photoluminescence spectrum of Glass Slide-UCNPs quenched by S protein with different concentration in swab (C) and in serum (F). Relative fluorescence signal of S protein with different concentration in swab (D) and in serum (G) under the magnetic modulation. Linear fit between the relative fluorescence signal and the lg concentration of S protein (from 0.1 ng/mL to 1000 ng/mL) in swab (E) and in serum (H). No significance (ns): $P > 0.05$, $*P \leq 0.05$, $**P \leq 0.01$, $***P \leq 0.001$, $****P \leq 0.0001$.

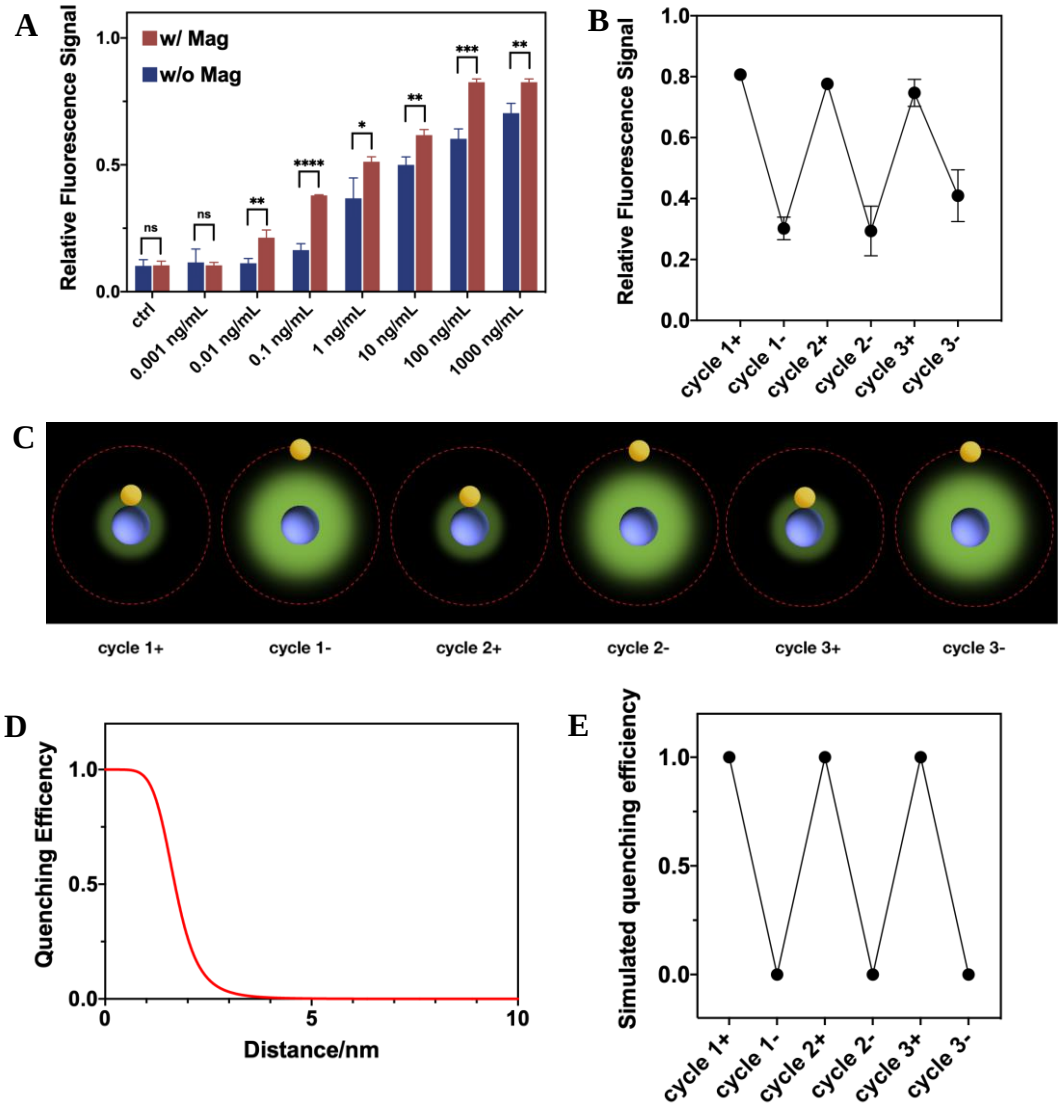

Fig. 5 The mechanism of the UCNP-based LRET biosensor. (A) Comparation of the relative fluorescence signal of S protein with different concentration with and without the magnetic modulation. No significance (ns): $P > 0.05$, $*P \leq 0.05$, $**P \leq 0.01$, $***P \leq 0.001$, $****P \leq 0.0001$. (B) The relative fluorescence signal of the magnetic field applied and reversed applied. (C) Illustration of the cycle of the magnetic modulation. (D) Finite-difference time-domain (FDTD) simulation of the relationship between the quenching efficiency and the distance between the UCNPs and the Fe_3O_4@Au Nps. (E) The cyclic quenching efficiency from the FDTD simulation.